

## Constraints on the diffuse high-energy neutrino flux from the third flight of ANITA

P. W. Gorham,<sup>1</sup> P. Allison,<sup>2</sup> O. Banerjee,<sup>2</sup> L. Batten,<sup>3</sup> J. J. Beatty,<sup>2</sup> K. Bechtol,<sup>4,5</sup> K. Belov,<sup>6</sup> D. Z. Besson,<sup>7,8</sup> W. R. Binns,<sup>9</sup> V. Bugaev,<sup>9</sup> P. Cao,<sup>10</sup> C. C. Chen,<sup>11</sup> C. H. Chen,<sup>11</sup> P. Chen,<sup>11</sup> J. M. Clem,<sup>10</sup> A. Connolly,<sup>2</sup> L. Cremonesi,<sup>3</sup> B. Dailey,<sup>2</sup> C. Deaconu,<sup>4</sup> P. F. Dowkontt,<sup>9</sup> B. D. Fox,<sup>1</sup> J. W. H. Gordon,<sup>2</sup> C. Hast,<sup>12</sup> B. Hill,<sup>1</sup> S. Y. Hsu,<sup>11</sup> J. J. Huang,<sup>11</sup> K. Hughes,<sup>4,2</sup> R. Hupe,<sup>2</sup> M. H. Israel,<sup>9</sup> K. M. Liewer,<sup>6</sup> T. C. Liu,<sup>11</sup> A. B. Ludwig,<sup>4</sup> L. Macchiarulo,<sup>1</sup> S. Matsuno,<sup>1</sup> C. Miki,<sup>1</sup> K. Mulrey,<sup>10,13</sup> J. Nam,<sup>11</sup> C. Naudet,<sup>6</sup> R. J. Nichol,<sup>3</sup> A. Novikov,<sup>7,8</sup> E. Oberla,<sup>4</sup> S. Prohira,<sup>7</sup> B. F. Rauch,<sup>9</sup> J. M. Roberts,<sup>1,14</sup> A. Romero-Wolf,<sup>6</sup> B. Rotter,<sup>1</sup> J. W. Russell,<sup>1</sup> D. Saltzberg,<sup>15</sup> D. Seckel,<sup>10</sup> H. Schoorlemmer,<sup>1,16</sup> J. Shiao,<sup>11</sup> S. Stafford,<sup>2</sup> J. Stockham,<sup>7</sup> M. Stockham,<sup>7</sup> B. Strutt,<sup>15</sup> M. S. Sutherland,<sup>2</sup> G. S. Varner,<sup>1</sup> A. G. Vieregge,<sup>4</sup> S. H. Wang,<sup>11</sup> and S. A. Wissel<sup>17</sup>

(ANITA Collaboration)

<sup>1</sup>*Department of Physics and Astronomy, University of Hawaii, Manoa, Hawaii 96822, USA*

<sup>2</sup>*Department of Physics, Center for Cosmology and AstroParticle Physics, Ohio State University, Columbus, Ohio 43210, USA*

<sup>3</sup>*Department of Physics and Astronomy, University College London, WC1E 6BT London, United Kingdom*

<sup>4</sup>*Department of Physics, Enrico Fermi Institute, Kavli Institute for Cosmological Physics, University of Chicago, Chicago, Illinois 60637, USA*

<sup>5</sup>*LSST, 950 North Cherry Avenue, Tucson, Arizona 85721, USA*

<sup>6</sup>*Jet Propulsion Laboratory, Pasadena, California 91109, USA*

<sup>7</sup>*Department of Physics and Astronomy, University of Kansas, Lawrence, Kansas 66045, USA*

<sup>8</sup>*Moscow Engineering Physics Institute, 115409 Moscow, Russia*

<sup>9</sup>*Department of Physics, McDonnell Center for the Space Sciences, Washington University, Saint Louis, Missouri 63130, USA*

<sup>10</sup>*Department of Physics, University of Delaware, Newark, Delaware 19716, USA*

<sup>11</sup>*Department of Physics, Graduate Institute of Astrophysics and Leung Center for Cosmology and Particle Astrophysics, National Taiwan University, 10617 Taipei, Taiwan*

<sup>12</sup>*SLAC National Accelerator Laboratory, Menlo Park, California 94025, USA*

<sup>13</sup>*Astrophysical Institute, Vrije Universiteit Brussel, Pleinlaan 2, 1050, Brussels, Belgium*

<sup>14</sup>*Center for Astrophysics and Space Sciences, University of California, San Diego, La Jolla, California 92093, USA*

<sup>15</sup>*Department of Physics and Astronomy, University of California, Los Angeles, Los Angeles, California 90095, USA*

<sup>16</sup>*Max-Planck-Institut für Kernphysik, 69117 Heidelberg, Germany*

<sup>17</sup>*Physics Department, California Polytechnic State University, San Luis Obispo, California 93407, USA*



(Received 26 April 2018; published 2 July 2018)

The Antarctic Impulsive Transient Antenna, a NASA long-duration balloon payload, searches for radio emission from interactions of ultrahigh-energy neutrinos in polar ice. The third flight of the Antarctic Impulsive Transient Antenna was launched in December 2014 and completed a 22-day flight. We present the results of three analyses searching for Askaryan radio emission of neutrino origin. In the most sensitive of the analyses, we find one event in the signal region on an expected background of  $0.7^{+0.5}_{-0.3}$ . Though consistent with the background estimate, the event remains compatible with a neutrino hypothesis even after additional postunblinding scrutiny.

DOI: [10.1103/PhysRevD.98.022001](https://doi.org/10.1103/PhysRevD.98.022001)

### I. INTRODUCTION

Ultrahigh-energy ( $>100$  PeV) neutrinos are expected to be produced from interactions of high-energy cosmic rays with cosmic microwave background photons [1]. The low expected flux [2] and small cross section require monitoring

an immense volume of a dense material for successful detection. Coherent Cherenkov emission in the radio regime (i.e., Askaryan emission [3]) from neutrino-induced showers in radio-transparent dense dielectric media such as ice provides a viable mechanism for achieving a large enough detector volume for the detection of the highest-energy

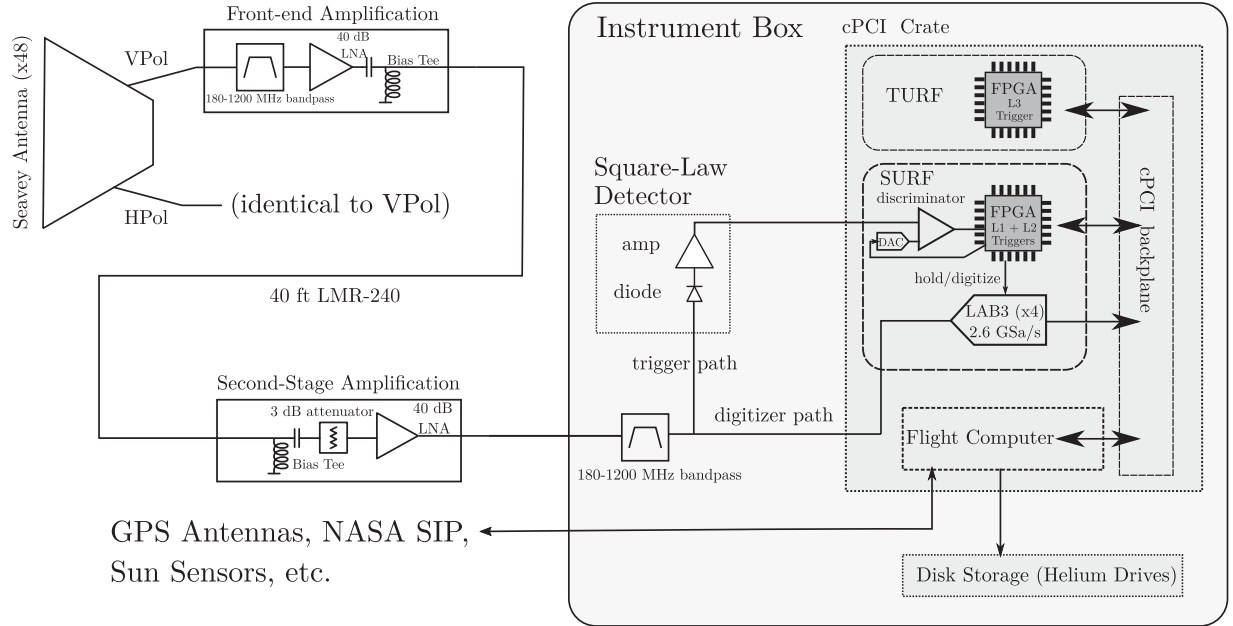


FIG. 1. A schematic diagram of the ANITA-III instrument. Signals from 48 dual-polarized, quad-ridge horn antennas are fed into a bandpass filter, through a low-noise amplifier, and then through a second-stage amplifier. Then, the signals are each split into two parts. The trigger path signal passes through a tunnel diode square-law detector and amplifier before being compared to a threshold that forms a first-stage (channel-level) trigger. If a global trigger (a coincidence between multiple channels) is issued, the signal from the digitizer path is digitized using a LAB3 switched capacitor array sampling at 2.6 GSa/sec, recorded on the flight computer and stored to a disk. The first levels of the trigger and digitization are performed by a custom board called a Sampling Unit for Radio Frequencies (SURF). The Trigger Unit for Radio Frequencies (TURF) collects lower-level trigger information from the entire payload to form global triggers. The NASA Support Instrument Package (SIP) is responsible for telemetry.

neutrinos. The expected signal is broadband up to a cutoff frequency of  $\sim$ GHz, and the emitted power scales quadratically with shower energy.

The Antarctic Impulsive Transient Antenna (ANITA), a NASA long-duration balloon payload [4], is an array of high-gain antennas that monitors the Antarctic ice sheet for impulsive, broadband neutrino, and cosmic-ray-induced radio emission. ANITA is not only sensitive to Askaryan emission from neutrino-induced showers in ice but can also observe geomagnetic emission from extensive air showers (EASs) induced by cosmic rays or decaying  $\tau$  leptons created by  $\tau$  neutrino interactions [5,6]. The analyses described here are optimized to look for neutrino-induced Askaryan emission but are also sensitive to the EAS channel. The EAS channel is a useful sideband region for these analyses, which is a region of phase space adjacent to the neutrino signal region, and useful for determining cut values and estimating efficiencies and backgrounds. Because of the direction of Earth's magnetic field in Antarctica, EAS emission is mainly horizontally polarized. Askaryan emission visible to ANITA is mostly vertically polarized for Standard Model cross sections, due to preferential Fresnel effects as the radio pulse propagates through the ice surface.

## II. EXPERIMENTAL TECHNIQUE

The third flight of the ANITA experiment (ANITA-III) launched on December 18, 2014. The instrument is similar

to the previous two ANITA payloads [7,8]. The primary upgrades from the second flight of ANITA (ANITA-II) are the addition of eight more antennas and a low-frequency antenna (ALFA) aimed at enhancing the detection of EAS signals, the implementation of a new impulsive full-band-only trigger in both horizontal and vertical polarizations, and the use of new lower-noise radio frequency amplifiers. Here, we briefly describe the instrument, flight, and calibration procedures.

### A. ANITA-III instrument

A schematic of the ANITA-III instrument and data acquisition system is depicted in Fig. 1. Forty-eight dual-polarization quad-ridge horn antennas from Antenna Research Associates, Inc., are arranged in a three-ring vertical cylindrical pattern to form 96 wideband (180–1200 MHz) channels. Each ring has 16 antennas, and each grouping of three antennas (top, middle, and bottom) is azimuthally aligned, forming 16 azimuthal sectors. The signal from each channel is bandpass filtered and then amplified by a custom-built low-noise amplifier, which is adjacent to the antenna, and then split into trigger and digitization paths after a second stage of amplification. Antenna temperatures are typically  $\sim$ 130 K, and the noise temperatures for the front-end filters and amplifiers are  $\sim$ 100 K.

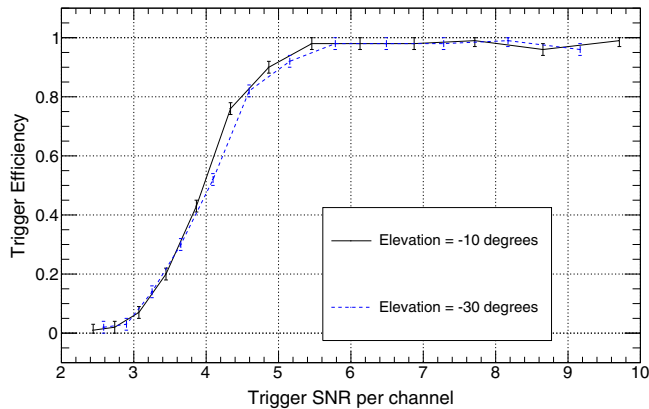


FIG. 2. Trigger efficiency vs voltage SNR, derived from lab measurements of injected signals in three adjacent azimuthal sectors. Efficiencies are shown for sets of delays between antennas corresponding to two different elevation angles.

The trigger path uses a custom tunnel diode as a fast square-law detector. The tunnel diode output is compared to a dynamically adjusted threshold to determine if a channel-level (first-level) trigger should be issued. Unlike previous ANITA payloads, first-level triggers are based solely on the total power within approximately 10 ns coincident windows in each channel, not the frequency content of the signal [4]. The trigger thresholds are adjusted in real time to keep the first-level trigger rate approximately at its target rate, which for ANITA-III was 450 kHz.

A second-level trigger condition is imposed at the level of each azimuthal sector and is satisfied by a coincidence of two or more channels in a single polarization within the sector. If a first-level trigger is issued for a given channel, a coincidence window opens during which another channel in the same azimuthal sector satisfying the first-level condition would generate a second-level trigger. The size of the coincidence window depends on the rings involved in the trigger, set by the expectation for up-going signals: 16 ns for the bottom ring, 12 ns for the middle ring, and 4 ns for the top ring.

The third-level (global) trigger is generated by the coincidence of second-level triggers occurring in the same polarization in adjacent azimuthal sectors. A global trigger will cause the digitized signals to be read out, assuming the four-deep digitizer buffer is not full. Over the course of the flight, the average dead time incurred from full digitizer buffers is 13%. Because the triggers for horizontal and vertical polarizations operate independently, it is possible to have a simultaneous trigger for both. The global trigger rate over the course of the flight for ANITA-III is approximately 50 Hz. The trigger efficiency as a function of the voltage signal-to-noise ratio (SNR) in the trigger chain, derived from lab measurements, is shown in Fig. 2. The trigger efficiency reaches 50% at a voltage SNR of  $4.0\sigma$ .

The digitizer path uses LAB3 [9] switched capacitor array digitizers with a mean sample rate of 2.6 GSa/s. Each channel has four 260-sample analog buffers to minimize dead time.

In addition to the science triggers generated by the trigger logic described above, there are triggers generated either by the payload computer or a pulse per second signal from the onboard GPS devices. These provide a set of minimum-bias triggers to help assess the noise environment during flight.

To prevent a portion of the payload from triggering too often and monopolizing all available digitizer buffers, a trigger mask is automatically enabled by the flight computer if an azimuthal sector's global trigger rate exceeds a configurable threshold. This allows ANITA to dynamically mask channels from the trigger that are subject at any given time to significant anthropogenic (man-made) noise from locations in Antarctica. Because of satellite interference in ANITA-III, throughout most of the flight, the channels that are North facing at a given time are masked.

The ANITA payload rotates freely. Two independent ADU5 differential GPS units are used to measure the payload attitude and position. Power is supplied and controlled with photovoltaic panels, a bank of batteries, and a charge controller. Telemetry is available during the flight through Iridium, TDRSS (when available), and a line-of-sight system when near McMurdo Station, the largest base of operations in Antarctica.

### B. ANITA-III flight

ANITA-III launched from the NASA long-duration balloon facility on the Ross Ice Shelf near McMurdo station on December 18, 2014. ANITA-III flew for 22 days before termination on January 9, 2015. The flight path is shown in Fig. 3. The hard disks and flight hardware were recovered with the aid of the Australian Antarctic Division from the nearby Davis station.

High-voltage impulsive calibration signals were sent to ANITA-III from the launch site and from an autonomous high-voltage calibration pulser deployed at west antarctic ice sheet Divide. These field pulsers are referenced to GPS time to facilitate identification. The data from the west antarctic ice sheet pulser proved particularly useful since ANITA-III passed close enough to be triggered over 100,000 times by the pulser.

ANITA requires extensive calibration of each digitizer in order to make full use of the precision timing information. In addition, a temperature correction must be applied to account for changes in clock frequency as a function of temperature. A detailed summary of these calibration procedures is provided in Refs. [11,12].

## III. ANALYSIS METHODS

Of the over 70 million science triggers captured during the ANITA-III flight, at most, a few events of neutrino

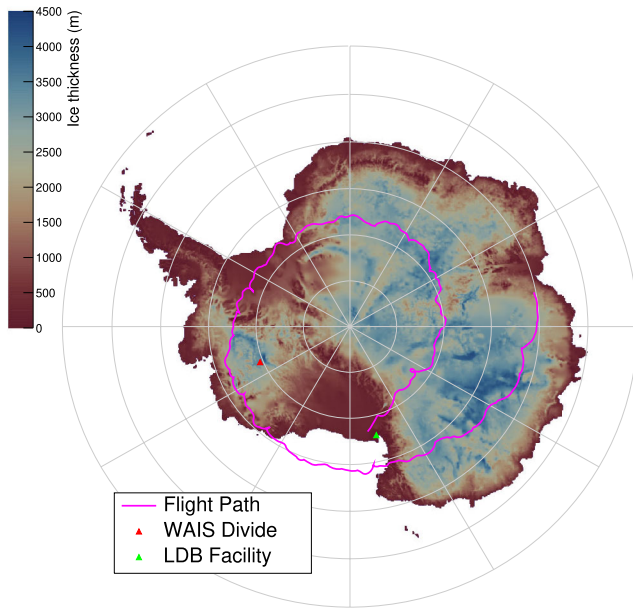


FIG. 3. The ANITA-III flight path is shown on top of a map of ice depth [10]. The location of a high-voltage radio impulse generator used as a calibration source (west antarctic ice sheet Divide) and the launch site (Long Duration Balloon Facility) are also shown.

origin are expected. The threshold-riding trigger on the instrument is set so that the vast majority of those events are thermal noise, the level of which in turn dictates ANITA’s threshold. The majority of the remaining events are anthropogenic transient and continuous-wave (cw) emission and occasional impulsive emission from the on-board electronics, which we call *payload blasts*.

After reviewing the backgrounds to the search and the simulation tools, we will briefly summarize the three neutrino searches performed. Additional detail for each analysis is provided in Appendixes.

### A. Classes of backgrounds

The vast majority of recorded ANITA-III events is random fluctuations of thermal noise due to ANITA’s threshold-riding trigger. The typical antenna temperature for ANITA-III is  $\sim 130$  K, from a combination of the sky and the ice that is in their field of view.

Anthropogenic CW from terrestrial transmitters or satellites will also trigger ANITA-III. In particular, the 260 and 380 MHz communication bands used by various satellites are a dominant cause of science triggers for ANITA-III. Even events that triggered on an impulsive neutrino-like signal can have a significant contribution from CW sources, which complicates analysis.

Self-triggered payload blasts are impulsive radio frequency emission generated by electronics on the ANITA payload. Although ANITA electronics are heavily shielded to prevent leakage of electromagnetic interference (EMI)

from the payload, some unknown source of self-interference still appears sporadically in the data. Payload blasts are characterized by nonplanar wavefront geometry (since they originate from very close to the antennas), a distinct frequency spectrum, and are typically much stronger in the bottom and middle rings of antennas than the top ring (also due to their being local to the payload).

Isolated, broadband impulsive anthropogenic emission from the ground and thermal noise fluctuations that by chance reconstruct as coming from the continent are both sources of background that remain after analysis cuts are developed. In all cases, the contribution to the expected background in the signal region is estimated before unblinding the search.

### B. Simulation

The primary ANITA simulation tool is ICEMC, described in detail in Ref. [13]. The ICEMC program includes a full treatment of the ANITA trigger and digitizer signal chain and uses the flight paths and recorded channel thresholds in order to model the acceptance of ANITA. It is a weighted Monte Carlo (MC), where each generated neutrino carries a weight corresponding to its survival probability and a phase-space factor.

We generate a set of simulated neutrinos to characterize the efficiency of the analyses. The simulated neutrinos follow the maximum mixed-composition Kotera *et al.* [2] flux model, hereafter referred to as “Kotera,” with Standard Model cross sections [14]. To simulate the flight noise environment, the trigger path was modeled with synthetic noise with levels and spectra derived from the flight, and real minimum-bias trigger data were added in the digitizer path. The choice of flux model has little effect on predicted neutrino observables. However, changes in neutrino interaction lengths, even within Standard Model bounds on cross section, affect what emission cones are visible, resulting in different observable angular and polarization distributions.

### C. Summary of blind searches

Three independent blind neutrino analyses were performed, which we denote, in order of completion, A, B, and C. Analyses A and B are similar to each other and to previous ANITA analyses in using common criteria across the continent and searching for isolated events [7,8]. Analysis C applies a new methodology in developing geographically dependent search criteria with the aim to maintain sensitivity even in regions of ice with higher levels of anthropogenic noise. Each neutrino search was done with at least one method of blinding: keeping hidden the region of parameter space where the signal resides, using a decimated data sample to set cuts, and/or “salting” the data by inserting simulated events. Further details are available in Appendixes A–C, respectively.

Each analysis begins by filtering waveforms to mitigate undesired CW contamination that would otherwise interfere with the analysis. Analyses A and B use an adaptive

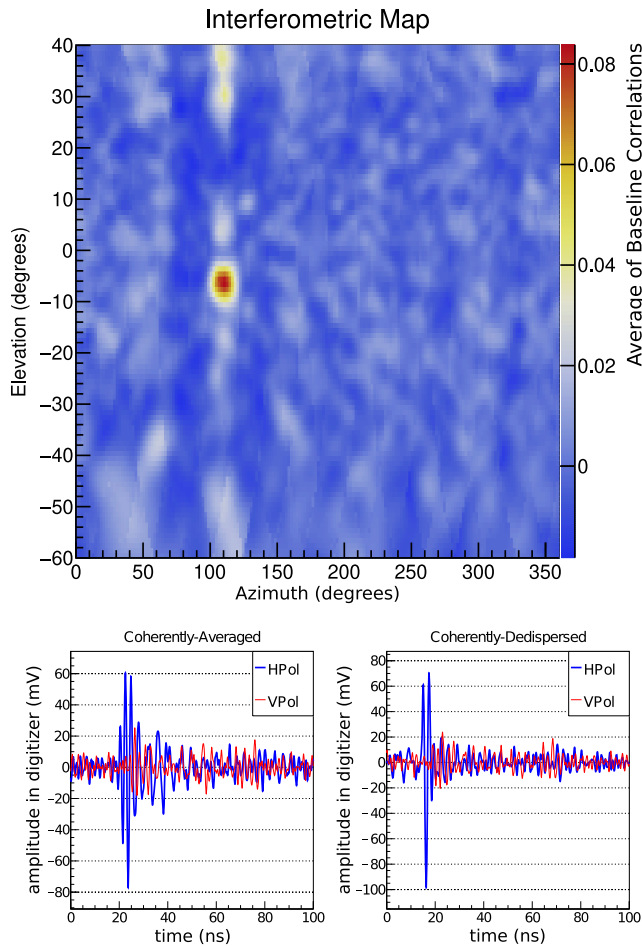


FIG. 4. An example of an interferometric map (top), a coherently averaged waveform (bottom left), and a dedispersed coherently averaged waveform (bottom right) for a calibration pulser event. The color scale in the top panel corresponds to the normalized cross-correlation value. Although we expect Askaryan neutrino signals to be mostly vertically polarized, the calibration pulser is horizontally polarized.

time-domain phasor removal technique, while C uses a method that removes CW phasors in the frequency domain [15].

The filtered waveforms from antennas with at least a partial common field of view are correlated against each other to produce an interferometric map [16], which indicates the apparent amount of correlated power as a function of incoming direction. Peaks of the map are considered hypotheses of coherent sources, for which a coherently averaged waveform is produced. The group delay of the instrument response can be removed from each waveform prior to coherent averaging, to form a dedispersed coherently averaged waveform. Figure 4 shows an example map, a coherently averaged waveform, and a dedispersed coherently averaged waveform for a calibration pulser event.

From the raw waveforms, the interferometric map, and coherent waveforms, each search computes a number of observables for each event that may be used to reject

backgrounds. Examples of observables include the peak correlation value of the interferometric map, the peak of a coherent waveform’s analytic envelope, measures of coherent and dedispersed waveform impulsivity, and polarimetric quantities. Each search has a set of “quality cuts” used to remove digitizer glitches, payload blasts, and other poor-quality events prior to attempting to separate thermal and anthropogenic backgrounds.

Analyses A and B use similar approaches to reject thermal and anthropogenic noise. A multivariate linear discriminant on various observables (different between the analyses, but much of the power in both is from measures of impulsivity) is used to discriminate signal-like events from background. This discriminant is trained with simulated events as a signal sample and events reconstructing above the horizontal as a nonimpulsive sideband. Events passing the signal selection are then spatially clustered in order to identify isolated signal-like events. Analysis A projects a bivariate Gaussian distribution corresponding to the pointing resolution for each passing event onto a map of Antarctica, creating a localization distribution on the continent, and considers the overlap of each event’s localization with the sum of the localizations of all other events, using no *a priori* information about human activity. Analysis B considers how close each event is to known locations of human activity (bases) or to the nearest other event that passes signal-like cuts, where a fit along the continent’s surface is used to find the best mutual location for each event pair. Both searches treat horizontally and vertically polarized events in the same way, but only passing vertically polarized events are in the Askaryan neutrino signal region. Passing horizontally polarized events contain a sample of EASs.

Analysis C is complementary in that it uses geographically dependent selection criteria to identify events that stand out from other events in the local noise environment. The power of this technique is in its ability to retain additional portions of the continent in the neutrino search in the presence of anthropogenic noise.

The search discretizes the continent, utilizing the HEALPix package [17], from the start, with each bin (about 400 km on a side) treated as an independent analysis. Cuts are optimized for the best expected limit after combining results across bins, reflecting bin-dependent neutrino sensitivities, noise environments, and systematic uncertainties on the background estimates.

Analysis C uses a 10% subset of the data to model the total background environment and assess the associated systematic uncertainties on the background estimates. Based on a common appearance of the background distributions across bins, we assert that the backgrounds follow an exponential behavior in a final cut variable. If an exponential fit in a bin gives a *p* value below 0.05, or insufficient data are available, the bin is rejected from the analysis. In addition to the systematic uncertainties that come from the fits, the optimization also accounts for a

systematic uncertainty due to the spillover of events between bins [18].

Analysis C utilizes cross-correlation values derived from both linearly and circularly polarized waveforms to reject thermal noise and events influenced by satellite interference [19]. Treating horizontal and vertical polarizations as separate search channels, Analysis C imposes a cut on a linear combination of the strength of the coherent waveform and the peak cross correlation that is bin dependent to distinguish thermal events from signal-like events.

Analyses A and B also set final thermal and clustering cuts by optimizing sensitivity. Analysis A estimates backgrounds with sidebands as in the on-off problem [20], avoiding the need to assert a model for the background distributions. Analysis B uses an on-off treatment for the anthropogenic background but an empirical model for the non-signal-like background. In both cases, events that reconstruct above the horizontal are used to estimate the leakage from the multivariate discriminant. To estimate the anthropogenic background, Analysis A uses a sideband that is subthreshold in the multivariate discriminant, while Analysis B uses a sideband of signal-like events near known bases. Analysis A has a total estimated background per polarization of  $0.8^{+0.6}_{-0.4}$ , and Analysis B expects  $0.7^{+0.5}_{-0.3}$  per polarization. Analysis C estimates backgrounds and uncertainties bin by bin that are about 0.1 event per bin with  $\sim 10\%$  systematic uncertainties.

The overall analysis efficiency, estimated using simulation, is  $72 \pm 5\%$  for Analysis A,  $84 \pm 3\%$  for Analysis B, and  $7^{+6}_{-3}\%$  for Analysis C, while Analysis C has more than twice its mean efficiency in some bins. Statistically, Analysis B is the most sensitive analysis.

Analyses A and B choose different clustering techniques to remove anthropogenic noise: Analysis A solely relies on event self-clustering and includes a larger event sample for clustering, while Analysis B relies on a list of known locations of human activity as well as event self-clustering. Analysis C aims to complement the other two searches by peering into noisy as well as quiet environments using geographically specific cuts, and with this aim in mind, more aggressively cut on backgrounds. Of the simulated neutrino events found by Analysis C, 25% of them would have been rejected by the other two analyses.

#### IV. RESULTS

Askaryan neutrino signals are expected to be predominantly vertically polarized for Standard Model cross sections, but all searches consider both horizontally and vertically polarized events. Horizontally polarized events are not in the Askaryan neutrino signal region, but they provide a useful cross-check on the analyses. Within the horizontally polarized sideband region are any events from EASs from cosmic rays and from  $\tau$  leptons originating from  $\nu_\tau$  interactions in the Earth or ice.

#### A. Summary of events found

The Askaryan neutrino search region is exclusively in the vertical polarization channel. However, we also report events identified by each analysis that pass all cuts except for the angle of linear polarization, which constitute a sample of horizontally polarized events that we use as a validation of the relative signal efficiencies reported in each analysis. We report on EAS candidate events in a separate paper [21].

Analysis A finds no events in the Askaryan signal region and 22 events in the horizontally polarized sideband. Of the 22, 21 are in agreement with the expected signal shape of an EAS template and have polarization consistent with the local geomagnetic field. The remaining event is inconsistent with an EAS hypothesis (it has both poor correlation with an EAS signal shape template and has nearly equal power in horizontal and vertical polarizations, which is not allowed by the Antarctic geomagnetic field) but is consistent with the background estimate of  $0.8^{+0.6}_{-0.4}$  in this horizontally polarized region. Eighteen of these events that are consistent with an EAS signature were identified in a separate, dedicated EAS search [12].

Analysis B identifies one event in the Askaryan neutrino signal region (event 83139414) and 25 events in the horizontally polarized sideband region. The event in the Askaryan neutrino signal region passed clustering cuts but was subthreshold in Analysis A. This is consistent with the slightly better analysis efficiency achieved by Analysis B compared to Analysis A. The 25 horizontally polarized events include 20 of the 21 events from Analysis A that are consistent with an EAS signature and five additional events, including one separately identified by the dedicated EAS search [12,21]. All horizontally polarized events that pass cuts in Analysis B are consistent with emission from EAS in both signal shape and polarization.

Analysis C identifies two vertically polarized events in the Askaryan neutrino signal region and seven horizontally polarized events that pass all cuts. Two of the horizontally polarized events (events 33484995 and 58592863) are also found in analyses A and B and are consistent with an EAS signature in the signal shape and polarization angle. A third (event 48837708) is also consistent with an EAS. The remaining four horizontally polarized events are consistent with the background estimate. The two events in the neutrino signal region are also consistent with the background estimate. We note that observing an event in each of two bins out of 37 has a negligible effect on the flux constraints and is one advantage of using a binned approach.

Table I lists all vertically polarized events that pass all cuts in at least one analysis. The locations of all horizontally polarized events consistent with EASs and the (vertically polarized) event in the Askaryan neutrino signal region identified by Analysis B are shown in Fig. 5. The total number of horizontally polarized events consistent

TABLE I. Summary of events identified by each search in the (vertically polarized) Askaryan neutrino search region. The analysis efficiencies on MC neutrinos and background estimates per polarization for each analysis are included. The one vertically polarized event remaining in the signal region in Analysis B was found to be subthreshold but isolated in Analysis A and was cut by a directional cut in Analysis C, discussed in Appendix C. All analyses find a number of events in the signal region consistent with their background estimates. A ✓ indicates that the event was found by a search. For events not identified, “Q” means the event was rejected by “quality” preselection cuts (e.g., requirements on trigger polarization, time, and *a priori* elevation angle cuts), an “S” means the event was subthreshold in a signal-like selection criteria, and a “P” indicates the event was rejected due to its position (clustering, or, for Analysis C, HEALPix bin or angular proximity to regions with geosynchronous satellites).

Identified by Analysis A			
Background estimate: $0.8^{+0.6}_{-0.4}$ per polarization			
Overall efficiency: $72 \pm 5\%$			
Event	A	B	C
...	...	...	...
Identified by Analysis B			
Background estimate: $0.7^{+0.5}_{-0.3}$ per polarization			
Overall efficiency: 84%			
Event	A	B	C
83139414	S	✓	P
Identified by Analysis C			
Expect $\sim 0.1$ event in each of 37 bins			
Efficiencies per bin: from a few % to 18%			
Event	A	B	C
21702154	S	S	✓
73750661	S	S	✓

with EASs observed (27) is consistent with the EAS results from the first flight of ANITA (ANITA-I), scaled for the relative exposures of the two flights [5].

### B. Limit on the diffuse neutrino flux and model constraints

The limit (Fig. 6) on the expected neutrino flux is calculated using a live time of 17.4 days and a geometric mean of ICEMC-computed acceptance with an acceptance estimate from an independent MC simulation developed for ANITA, the analysis efficiency as a function of neutrino energy, and the appropriate 90% Feldman-Cousins factor for the number of events detected and expected backgrounds. Further details are available in Appendix D. While Analysis A would provide the best limit (as it finds no events), Analysis B has the best expected sensitivity, so we use its result to set the limit. The expected number of events for the Kotera maximum mixed-composition and maximum all-proton models are  $0.029 \pm 0.002$  and  $0.17 \pm 0.01$ , respectively. ANITA-III sets a 90% C.L. integral flux limit on a pure  $E_\nu^{-2}$  spectrum for  $E_\nu \in [10^{18} \text{ eV}, 10^{21} \text{ eV}]$  of  $E_\nu^2 \Phi_\nu \leq 4.6 \times 10^{-7} \text{ GeV cm}^{-2} \text{ s}^{-1} \text{ sr}^{-1}$ .

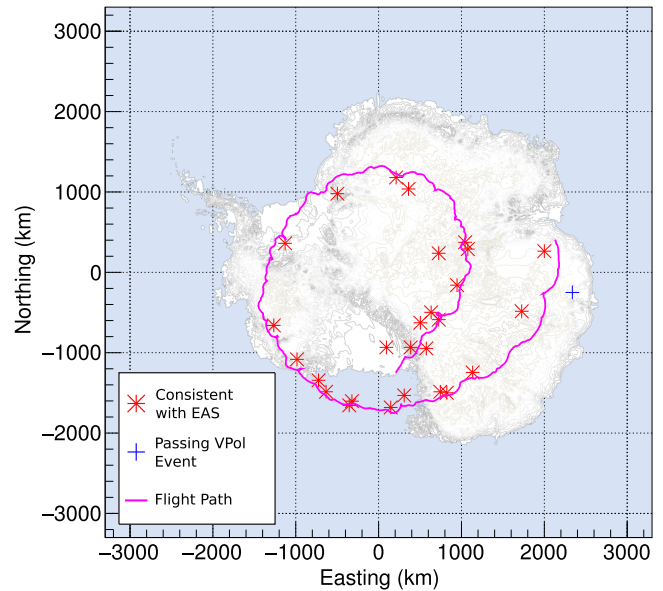
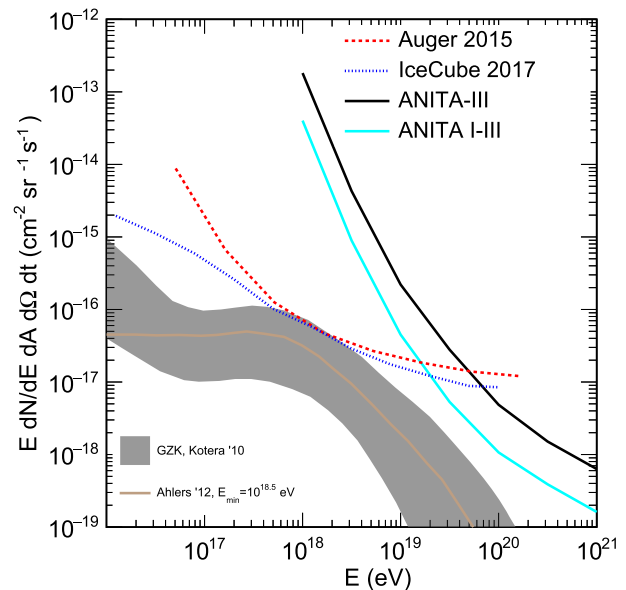


FIG. 5. Events consistent with EASs from Analyses A, B, and C and the event in the vertically polarized Askaryan neutrino signal region from Analysis B (the most efficient of the three analyses). Only horizontally polarized events with a good EAS template correlation match, and consistent polarization with the local geomagnetic field are shown on the map.



$\log_{10}(E(\text{eV}))$	18	18.5	19	19.5	20	20.5	21
A ( $\text{km}^2 \cdot \text{sr}$ )	0.00038	0.016	0.31	2.5	14	46	109

FIG. 6. ANITA-III limit on the all-flavor-sum diffuse ultrahigh-energy neutrino flux and a combined limit from ANITAs I–III, using the ANITA-III limit shown here and the published ANITA-II and ANITA-I limits [7,8]. The latest ultrahigh-energy neutrino limits from the Auger [22] and IceCube [23] experiments and two cosmogenic neutrino models [2,24] are also shown. See Appendix D for details about the calculation of the limit. The table lists the ANITA-III effective area as a function of neutrino energy used to make the limit, not including analysis efficiency.

We also show a combined limit from ANITA I-III, in which we have used the total number of events seen, total expected background, and the analysis-efficiency-weighted sum of previously published effective volumes [8].

## V. DISCUSSION

The isolated vertically polarized event 83139414 from Analysis B (and just outside the signal region in A) is particularly intriguing. While consistent with the preunblinding background estimate, our postunblinding interpretation is that the event is both unusually isolated and has a signal shape (Fig. 7) consistent with impulsive broadband emission. There is no known human activity within 260 km.

The polarization of the surviving event is consistent with expectations from neutrino simulations, and the signal has no features that make it easily identifiable as an anthropogenic signal (e.g., slow rise time, narrow bandwidth, or double-pulse structure). Including additional metrics such as these to distinguish neutrino-like signals from anthropogenic noise would reduce a postunblinding background estimate for this particular event by an order of magnitude.

The emission comes from a location on the continent consistent in ice depth and elevation angle with simulated distribution of neutrinos. The source location of the emission is fully consistent with MC neutrinos simulations with the ANITA-III flight path and recorded thresholds. Simulations of neutrinos near the interaction location with the payload near the detection position suggest a minimum

possible neutrino energy of  $10^{19}$  eV. Simulation may also be used to estimate the direction of a neutrino producing radio emission compatible with the observed location and polarization. The localization corresponding to the surviving event in equatorial coordinates is well approximated by an elliptical Gaussian centered at (RA, dec) = (11.43 h, 16.3°), with major and minor axis standard deviations of 5.0° and 1.0°, respectively, and a position angle of 73.7°.

In summary, despite challenging EMI conditions ANITA-III has yielded a robust sample of radio-detected ultrahigh-energy cosmic rays [21]. While no compelling neutrino signal above background has been detected, the one remaining passing event in Analysis B is rather unlike the parent anthropogenic population that comprises the typical background but shares several important characteristics expected from neutrino events.

## ACKNOWLEDGMENTS

We would like to thank the NASA and the National Science Foundation. We would especially like to thank the staff of the Columbia Scientific Balloon Facility and the logistical support staff enabling us to perform our work in Antarctica. We are deeply indebted to those who dedicate their careers to help make our science possible in such remote environments. This work was supported by the Kavli Institute for Cosmological Physics at the University of Chicago. Computing resources were provided by the University of Chicago Research Computing Center and the Ohio Supercomputing Center at The Ohio State University. A. C. would like to thank the National Science Foundation for their support through CAREER Grant No. 1255557. O. B. and L. C.'s work was also supported by collaborative visits funded by the Cosmology and Astroparticle Student and Postdoc Exchange Network. The University College London group was also supported by the Leverhulme Trust. The Taiwan team is supported by Taiwan Ministry of Science and Technology under its Vanguard Program No. 106-2119-M-002-011.

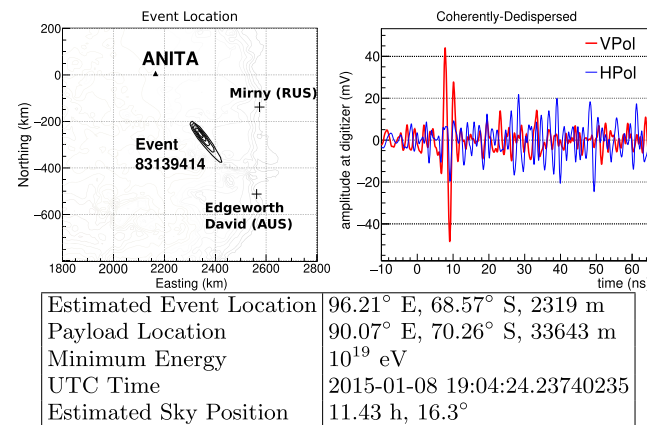


FIG. 7. Event localization (left) and dedispersed coherently averaged waveform (right) for vertically polarized event 83139414. This event is in the Askaryan neutrino signal region in Analysis B and a subthreshold, isolated event in Analysis A. The table below provides additional information about the event: the longitude, latitude, and ice depth at the estimated event location; the longitude, latitude, and altitude of payload at time of detection; and the minimum neutrino energy and mean sky position that could have produced the event according to the MC simulation. The black contours on the map represent 1–5 $\sigma$  regions for the event location.

## APPENDIX A: ANALYSIS A

### 1. Filtering and interferometry

The first step in Analysis A is to mitigate man-made, narrow-frequency transmitter contamination in each channel. Such sources are referred here as CW. We use the power spectrum to iteratively identify the highest-power frequency, which constrains a trial sinusoidal fit in the waveform that we then subtract.

We use these filtered waveforms and interferometry to generate the pointing map for each event, following the procedure in Ref. [16]. We cross-correlate pairs of nearby antennas (normalized by power) to extract time delays that in turn allow pointing. The procedure is applied to every point on the sky to make a map. We consider the largest

three isolated map peaks in each polarization as source candidates. We extract azimuth ( $\phi$ ) and elevation ( $\theta$ ) using a quadratic fit to make a higher-resolution map near the peaks.

## 2. Signal-like event selection

For each candidate source, we compute a ‘‘coherent waveform’’ by adding all channels with the proper delay. We also compute a ‘‘dedispersed coherent waveform’’ using the measured instrument response and antenna response from that direction. We introduce an impulsivity measure,  $\mathcal{I}$ , by considering the average,  $A$ , of the cumulative distribution of the fractional power contained within a time before or after the peak of the Hilbert envelope (the magnitude of the analytic signal). We define  $\mathcal{I}$  as  $2A-1$ . We choose the source candidate with the largest  $\mathcal{I}$  for further analysis.

We first require that the payload triggered on the polarization of the most impulsive candidate. The second cut removes events with channel amplitudes exceeding 1.0 V to remove digitizer glitches and saturating events.

The third cut targets payload-generated impulses (‘‘payload blasts’’), which originate from the payload and are impulsive, but are not the expected plane waves from distant sources. To remove these local events, we use a set of cuts that requires that all rings of antennas have comparable power and in which the peak of the coherent average is compatible with the average of the individual waveforms that comprise it.

The fourth cut aims to distinguish signal-like waveforms, with power to separate from thermal noise, any CW surviving the filtering process and any payload blasts that survive at this stage. A Fisher discriminant [25] is used with the following observables: 1) normalized average correlations, 2) the angular distance between reconstructed azimuth and mean trigger direction, 3) Hilbert envelope peak of the dedispersed average, 4) the difference between the average of individual waveform peaks and the coherent average peak, 5)  $\mathcal{I}$  for the dedispersed average, 6) the difference of squares of the  $\mathcal{I}$  s of dedispersed average and coherent average, 7) the power-normalized difference between the peak of the dedispersed average and the coherent average, 8) the full-waveform linear polarization fraction, 9) the near-peak linear polarization fraction, and 10) the change in peak time between coherent and dedispersed averages.

The discriminant is trained with the Toolkit for Multivariate Data Analysis with ROOT [26] framework using the signal sample of simulated neutrinos and a background sample populated by events in which the most impulsive candidate reconstructs above the horizontal plane. The distributions of the multivariate analysis discriminator value,  $\mathcal{F}$ , for the two samples is shown in Fig. 8. The impulsivity variables dominate the power of the discriminant.

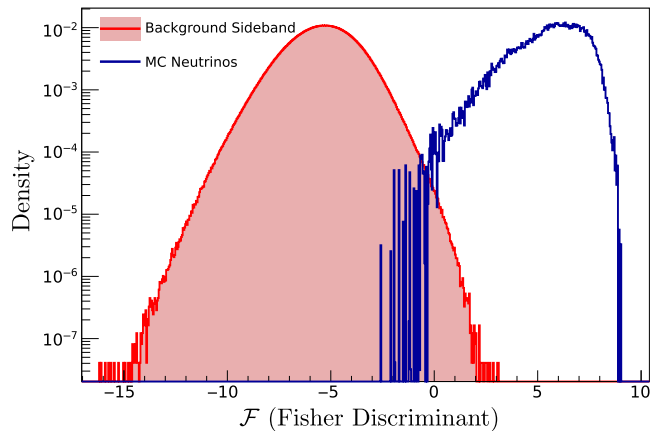


FIG. 8. Distributions of the multivariate score,  $\mathcal{F}$ , for weighted simulated neutrinos (blue) and the sideband reconstructing above the horizontal plane (red) we use as a background sample to train the Fisher discriminant used in Analysis A.

## 3. Isolation parameter (clustering)

The final cut requires events to be spatially isolated to separate neutrino-like events from anthropogenic events, which are likely to cluster with themselves. We localize each plane-wave event (i.e., not thermal noise or payload blasts) reconstructed by ANITA to a particular direction in payload coordinates,  $(\phi_0, \theta_0)$  with an uncertainty we model as a bivariate Gaussian distribution,  $\mathcal{P}(\phi, \theta | \sigma_\phi, \sigma_\theta)$ . We estimate  $\sigma_\phi$  and  $\sigma_\theta$  using the measured pointing resolution from calibration pulsers, with corrections for heading uncertainty and elevation angle.

This distribution  $\mathcal{P}(\phi, \theta)$  projected onto Antarctica is called  $\mathcal{P}'(E, N)$ . We exclude portions of  $\mathcal{P}$  that miss the ground and renormalize the distribution. We exclude events with less than 0.1% of  $\mathcal{P}$  on the continent or with elevation more than  $40^\circ$  below the horizontal plane. We then compare  $\mathcal{P}'$ , which is an event’s localization distribution, to that of other events.

The well-known Bhattacharyya coefficient [27],  $BC(p_i(\vec{x}), p_j(\vec{x})) = \int \sqrt{p_i p_j} d\vec{x}$ , quantifies the similarity of the two distributions. We extend this general idea to compute a global overlap,  $\mathcal{O}$ , of each event,  $i$ , with all other events of interest,  $j$ , as

$$\mathcal{O} = \sum_j \int_{\text{Antarctica}} \sqrt{w_i w_j \mathcal{P}'_j \mathcal{P}'_i}, \quad (\text{A1})$$

where  $w$  is a weighting factor. An event originating near many other events of interest will have a large  $\mathcal{O}$ , while an isolated event has  $\mathcal{O} \approx 0$ . The variable  $\mathcal{O}$  spans many orders of magnitude, so it is convenient to work with  $-\log \mathcal{O}$  as an isolation parameter.

The sample of events used for clustering is defined using the Fisher score  $\mathcal{F}$ . We find that there is a change in the shape of the background sample distribution along the Fisher score at  $\mathcal{F} > 2$ , so we include all events above that score in the

clustering sample. Between  $\mathcal{F} > 2$  and  $\mathcal{F} < 3.2$ , where we ultimately set our final cut on  $\mathcal{F}$  that defines the signal region, we assign a weight between 0 and 1 in the clustering sample based on the  $\mathcal{F}$  value, with a weight of 1 for events at  $\mathcal{F} = 3.2$  and a weight of 0 for events at  $\mathcal{F} = 2$ . Above  $\mathcal{F} = 3.2$ , we assign a weight of 1 for each event.

#### 4. Setting final cut values

The final cut thresholds for  $\mathcal{F}$  and  $-\log \mathcal{O}$  are set to optimize the sensitivity of the Askaryan neutrino search on the Kotera flux model. We compute the analysis efficiency using simulated neutrinos generated according to a Kotera flux model and passing them through the analysis. For the isolation cut, each neutrino is individually evaluated against the entire source map. We estimate a 5% systematic uncertainty on analysis efficiency based on a comparison with the calibration pulsers deployed on the ice.

The two sources of background, leakage from events cut by the Fisher discriminant ( $\mathcal{B}_{\mathcal{F}}$ ) and leakage from isolated anthropogenic signal-like events ( $\mathcal{B}_{\mathcal{O}}$ ), are each estimated from background regions, as in the on-off problem. We estimate  $\mathcal{B}_{\mathcal{F}}$  from the above-horizontal background region depicted in Fig. 8. We calculate the leakage in the background region and multiply by the ratio of events in the background to those below the horizon.

We lack a true signal-free background region to estimate  $\mathcal{B}_{\mathcal{O}}$ . We instead use the subthreshold region  $\mathcal{F} \in (2, 2.8)$ , where the upper threshold remains below any reasonable cut in  $\mathcal{F}$  to avoid accidental unblinding, and use the distribution of events in this region in  $-\log \mathcal{O}$  to estimate the background in the region of interest. We consider events in both polarizations but exclude large clusters.

We use a profile-likelihood method [20] implemented with ROOSTATS [28] to optimize the final cut on  $\mathcal{F}$  and  $-\log \mathcal{O}$ . Using this model, we find the search to be most sensitive with a cut on  $\mathcal{F} > 3.2$  and  $-\log \mathcal{O} > 12$ .

Each polarization is expected to contribute equally to background. The total estimated background from all sources for this search in either the horizontal or vertical polarization region is  $0.78^{+0.60}_{-0.39}$ .

Figure 9 shows the clustering efficiency of MC neutrino events surviving preclustering cuts as a function of position on the continent. The analysis efficiency is 88% preclustering and 72% after all cuts are applied.

#### 5. Results

After unblinding, zero events were found in the vertically polarized signal region. This corresponds to a 90% upper limit on triggered neutrino events of 1.37 using the prescription outlined before and 1.67 using a standard Feldman-Cousins method integrated over systematics. While not in the signal region, there was one isolated, vertically polarized event (83139414,  $\mathcal{F} = 3.1$ ) below the final cut threshold on  $\mathcal{F}$ , which was a broadband, impulsive, isolated event. This is the same event found in Analysis B and depicted in Fig. 7.

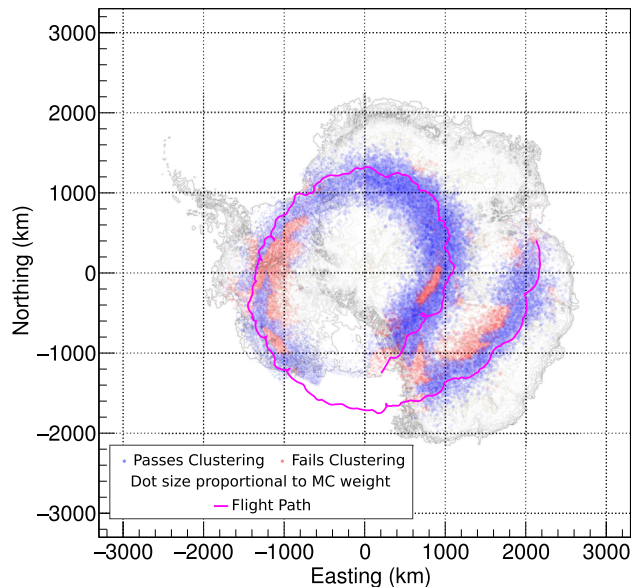


FIG. 9. Clustering efficiency on simulated neutrinos in Analysis A. Each dot represents a MC neutrino event passing preclustering cuts, with the area scaled to MC weight. Blue points indicate events that pass clustering after removing likely extensive air showers; red points are those that fail clustering.

In the horizontally polarized channel, 22 events were found in the signal region, 21 of which had a waveform shape and polarization consistent with geomagnetic emission from EASs created by cosmic rays. The other was inconsistent with the EAS hypothesis (in both shape and polarization) but was consistent with our background estimate. Eighteen of these events were also found in a dedicated air shower search [12] that used an independent method relying on cross-correlation with a waveform template from a cosmic-ray simulation.

Table II shows the effect of each cut on the data and on simulated neutrinos.

TABLE II. The effect of each cut on horizontally polarized (HPol) and vertically polarized (VPol) science triggers as well as the efficiency of each cut on MC-generated neutrinos for Analysis A. The bottom row in the table shows the remaining events in the horizontally and vertically polarized signal regions as well as the total analysis efficiency after all cuts are applied.

Cut	MC $\nu$ efficiency	VPol remaining	HPol remaining
None	1.00	38 274 132	36 700 502
Trigger correct polarization	0.98	20 599 991	18 825 981
Peak <1000	0.96	20 565 939	18 811 772
Payload blast	0.95	16 474 185	15 655 493
Elevation <0	0.95	3 821 760	3 802 329
$\mathcal{F} > 3.2$	0.88	169 824	311 795
$-\log \mathcal{O} > 12$	0.72	0	22

TABLE III. Events passing cuts in sequence in Analysis B, similar to Table II for Analysis A. The final total of vertically polarized events is given after removing inserted events.

Cut	MC $\nu$ efficiency	VPol remaining	HPol remaining
Not ground pulser	1.00	8 888 370	10 767 799
Close to MC truth	0.99		
Quality cuts	0.97	8 125 293	9 940 345
Pass thermal cut	0.96	242 957	361 383
Not HiCal	0.95	242 941	360 604
Clustering	0.84	1	25

## APPENDIX B: ANALYSIS B

### 1. Blinding

Analysis B, like Analysis A, did not look in the hidden signal region until all cuts were set. Additionally, a small number (unknown to the analyst) of vertically polarized calibration pulser events were inserted randomly throughout the data. These were removed after opening the blinded region. No horizontally polarized events were inserted.

### 2. Filtering, reconstruction, and quality cuts

Analysis B uses the same filtering method as Analysis A and a similar reconstruction method (Appendix A 1). Unlike Analysis A, we use the source candidate with the largest map peak value,  $\mathcal{P}$ , to define the event direction,  $\phi_{\mathcal{P}}, \theta_{\mathcal{P}}$ , and primary polarization.

We restrict the analysis sample to events with  $\theta_{\mathcal{P}} < 0$  and remove ground station calibration pulses from the data set using subsecond timing information.

We first remove the small subsample of data that is poorly recorded or reconstructed by requiring good GPS data, sufficient samples in the digitized waveforms, and consistent pointing ( $\theta_{\mathcal{P}}, \phi_{\mathcal{P}}$ ) at each stage of the directional reconstruction (Appendix A 1).

We then use a series of cuts to remove payload blasts. We remove events that do not have similar power or peak amplitude in the top and bottom antenna rings. Events in which the Hilbert envelope peak,  $\mathcal{H}$ , does not scale as expected with the top and bottom antenna ring amplitudes or map peak,  $\mathcal{P}$ , are also removed. The effect of these cuts on the data and a Kotera flux of simulated neutrinos is given by the “quality cuts” row in Table III.

### 3. Impulsivity cuts

Like Analysis A, Analysis B trains a Fisher discriminant,  $\mathcal{F}$ , to separate simulated neutrino events from a nonimpulsive background region consisting of triggered events with ( $\theta_{\mathcal{P}} > 0$ ).

The Fisher discriminant  $\mathcal{F}$  is a weighted sum of seven variables: the map peak,  $\mathcal{P}$ ; the Hilbert envelope peak of

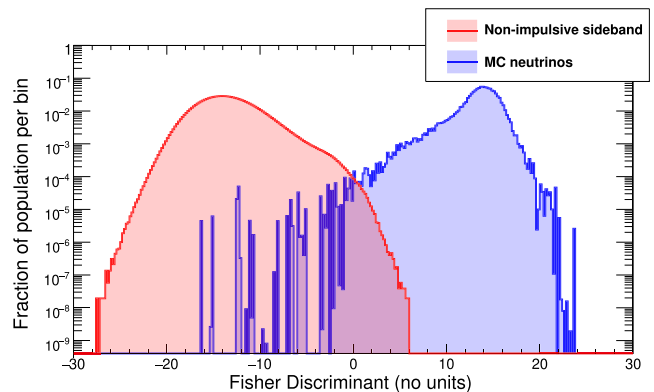


FIG. 10. The distribution of the Analysis B Fisher discriminant,  $\mathcal{F}$ , for the nonimpulsive background region and simulated neutrinos.

the coherently averaged waveform before ( $\mathcal{H}_{\mathcal{C}}$ ) and after ( $\mathcal{H}_{\mathcal{D}}$ ) dedispersion; and Analysis A’s impulsivity measure before ( $\mathcal{I}_{\mathcal{C}}$ ) and after ( $\mathcal{I}_{\mathcal{D}}$ ) dedispersion. Analysis B uses a new variable, the power window gradient,  $\mathcal{G}$ , defined as the average difference between the five smallest time windows containing 10%, 20%, 30%, 40%, and 50% of the total power. The final two components of  $\mathcal{F}$  are  $\mathcal{G}_{\mathcal{D}}$  and  $\mathcal{G}_{\mathcal{C}}/\mathcal{G}_{\mathcal{D}}$ , where the subscripts  $\mathcal{C}$  and  $\mathcal{D}$  correspond to the coherently averaged waveform before and after dedispersion, respectively. The distributions of  $\mathcal{F}$  are shown in Fig. 10.

To remove nonimpulsive events from the analysis sample, we require  $\mathcal{F} > 5.8$ . We model the tail of the nonimpulsive background region as an exponential, fitting over a range of tail values. The cut was set such that we expect fewer than 0.5 events in the search region, by multiplying the number of expected events above the cut in the background region by the ratio of events in the background region to the search region. We treat each polarization symmetrically and estimate a nonimpulsive background of  $0.16 \pm 0.01$  events per polarization.

We remove calibration pulser events from HiCal [29], a balloon-mounted calibration pulser, with an azimuth pointing cut  $|\phi_{hc} - \phi_{\mathcal{P}}| < 5^\circ$ , where  $\phi_{hc}$  is the azimuth of HiCal in ANITA payload coordinates.

The effect of these cuts for events passing quality cuts is given in Table III.

### 4. Clustering algorithm

For each event, we project the best direction hypothesis along payload coordinates ( $\phi_{\mathcal{P}}, \theta_{\mathcal{P}}$ ) onto a model of the Antarctic surface [10]. To group surviving events together, we use a clustering algorithm with two metrics: Euclidean separation on the surface and an angular separation at the payload. Events  $i$  and  $j$  belong to the same cluster if their Euclidean separation  $d_{ij} \equiv |\vec{x}_i - \vec{x}_j| < \lambda$ , where  $\lambda$  is a threshold distance. For the angular clustering, we perform a fit for each pair of events  $i, j$ , to minimize a “same-source likelihood,”  $L(\vec{s})_{ij}$ , given by

$$-2 \log(L(\vec{s})_{ij}) = \left( \frac{\theta_i - \theta_{si}}{\sigma_{\theta_i}} \right)^2 + \left( \frac{\phi_i - \phi_{si}}{\sigma_{\phi_i}} \right)^2 + \left( \frac{\theta_j - \theta_{sj}}{\sigma_{\theta_j}} \right)^2 + \left( \frac{\phi_j - \phi_{sj}}{\sigma_{\phi_j}} \right)^2. \quad (\text{B1})$$

The fit varies a position on the surface,  $\vec{s}$ , which appears at payload coordinates  $(\phi_{si}, \theta_{si})$  for event  $i$ . The event  $i$  angular resolution,  $\sigma_{\phi_i}$  and  $\sigma_{\theta_i}$ , is estimated from the resolution of calibration pulse events with the same SNR. Events  $i, j$  are considered clustered if  $-2 \log(L(\vec{s})_{ij}) < \Lambda$ , where  $\Lambda$  is an angular threshold.

### 5. Base association

We obtained a list of bases active in 2014–2015 by correspondence with a variety of Antarctic national programs. We exclude regions surrounding each base using the same metrics as the event-event clustering (Appendix B 4). A cluster of events is associated with a base,  $b$ , if their separation  $d_{ib} = |\vec{x}_i - \vec{x}_b| < \lambda$ . A cluster is also associated with a base if the angular separation,  $-2 \log(L)_{ib}$ , of any event  $i$  satisfies

$$-2 \log(L)_{ib} = \left( \frac{\theta_i - \theta_b}{\sigma_{\theta_i}} \right)^2 + \left( \frac{\phi_i - \phi_b}{\sigma_{\phi_i}} \right)^2 < \Lambda, \quad (\text{B2})$$

where  $(\phi_b, \theta_b)$  is the location of base  $b$  in payload coordinates for event  $i$ .

### 6. Setting clustering thresholds

We estimate an anthropogenic background from the possible incompleteness of our base list using an *ABCD* method, in which  $A$  is the number of small multiplets associated with known bases,  $B$  is the number of small multiplets *not* associated with known bases,  $C$  is the number of singlets associated with known bases, and  $D$  is the number of singlets not associated with known bases (signal region).  $D$  is estimated as

$$D = C \times \frac{B}{A}. \quad (\text{B3})$$

The values of  $A, B, C,$  and  $D$  depend on  $\lambda$  and  $\Lambda$ . They also depend on the location of the inserted events (Appendix B 1). If the clustering is efficient, most inserted events will end up in category  $D$ . However, if any end up in  $A, B,$  or  $C$ , it will change the background estimate. To set the clustering thresholds, we make an initial background estimate (to be revised in the case in which any inserted events are found in category  $A, B,$  or  $C$  after opening the box) by defining a “small multiplet” as containing two to four events and without modeling any uncertainty on the size of the known activity background region  $\tau_{abcd} = A/B$ .

Similar to Analysis A (Appendix A 4), we use a profile-likelihood method [20] implemented with ROOSTATS [28]

to choose  $\lambda$  and  $\Lambda$  to maximize sensitivity to a Kotera flux of neutrinos. We perform a scan through  $1 \leq \Lambda \leq 4000$  with  $\lambda = 30, 40, 50$  km, finding  $\lambda = 40$  km and  $\Lambda = 4$  give the best sensitivity. Applied to simulation, the neutrino clustering efficiency is 89%, and when applied after the impulsivity cuts, the total analysis efficiency is 84%. We estimate a 3% systematic uncertainty on the efficiency based on a comparison with calibration pulsers. The provisional background estimate from clustering alone (vertical and horizontal polarizations together) is 0.67 events.

### 7. Analysis B results

After unblinding, Analysis B finds 25 horizontally polarized events and 13 vertically polarized events, of which 12 were inserted as a form of blinding (Appendix B 1). The distribution of impulsive events from the continent with simulated neutrinos passing and failing clustering cuts is shown in Fig. 11. The 12 inserted events that passed the analysis have been removed.

There were 14 inserted vertically polarized events in total, giving an inserted event efficiency of 85%, which is consistent with the efficiency estimate from the simulation. The two inserted events that failed the analysis clustered with one another in a nonbase multiplet of size 2, falling into category  $B$  in Eq. (B3). After removing these events, we reestimate the anthropogenic background, accounting for two additional sources of uncertainty not considered in Appendix B 6. We allow the known-base background region

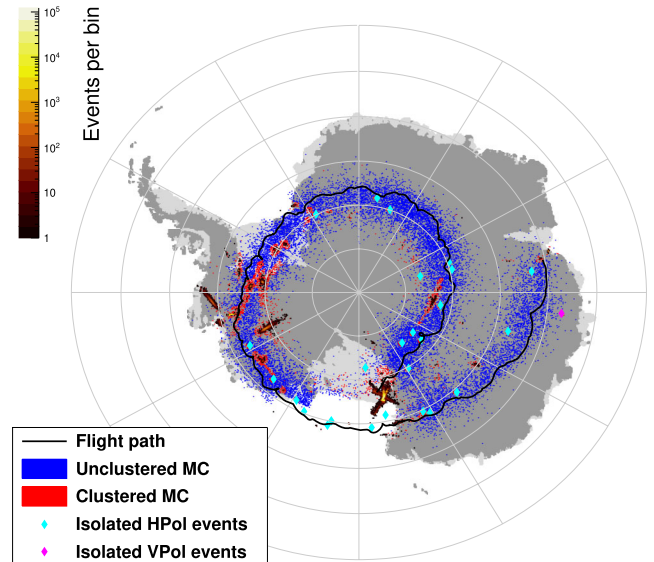


FIG. 11. The histogram shows all events passing preclustering cuts in analysis B projected onto the continent along with a subset of the simulated neutrinos passing (blue) and failing (red) clustering cuts. The positions of the 25 isolated horizontally polarized (cyan) and vertically polarized (magenta) events are also shown.

ratio,  $\tau_{abcd} = A/B$  [from Eq. (B3)] to vary by changing the upper limit on small multiplets (Appendix B 5) from 4 to 9. Additionally, we construct a distribution for  $D$  by drawing from three Poisson distributions with means  $A$ ,  $B$ , and  $C$ . The updated background estimate was divided equally between horizontal and vertical polarizations by setting  $\tau_{abcd}(\text{VPol}) = \tau_{abcd}(\text{HPol}) = 2\tau_{abcd}$ . This led to an anthropogenic background estimate of  $0.50^{+0.50}_{-0.25}$ .

Having combined this estimate with the nonimpulsive background estimate (Appendix B 3), the final result of Analysis B is 25 horizontally polarized events, all consistent with emission from cosmic-ray air showers, on an expected background of  $0.7^{+0.5}_{-0.3}$ , and one vertically polarized event in the Askaryan neutrino signal region on an expected background of  $0.7^{+0.5}_{-0.3}$ . Details of the events are discussed in Sec. IV.

### APPENDIX C: ANALYSIS C

Analysis C imposes geographically dependent selection criteria that are designed to be optimal for the local noise environment. This approach has the potential to recover sensitivity in regions of ice rejected in clustering-based searches and reach lower thresholds in regions of ice that are free of anthropogenic backgrounds.

#### 1. Cuts based on circular polarization and the linear discriminant cut

Analysis C is unique in performing event reconstruction in circular polarization. Being linearly polarized, the Cherenkov emission from neutrinos is expected to show strong cross-correlation in both circular polarizations for relative delays corresponding to the incoming radio frequency direction, unlike thermal noise and satellite CW signals. ANITA-III observed CW emission from geosynchronous satellites with a strong left circular polarization (LCP) component. In Fig. 12, we plot the ANITA payload longitude on the vertical axis and the reconstruction in azimuth of events in LCP on the horizontal axis, with color representing the number of events. Distinct overdensities or “stripes” can be seen with the slope expected for geosynchronous orbits.

To select linearly polarized signals, based on an optimization for the best expected limit at an early stage of the analysis, we remove events with a cross-correlation peak in LCP greater than  $46^\circ$  from that in right circular polarization and with the peak-normalized cross-correlation value in either circular polarization below 0.015. These cuts predominantly remove thermal noise rather than satellite interference. We also reject events of which the LCP reconstruction map peaks in a direction corresponding to one of the stripes seen in Fig. 12, if a geostationary satellite at a given azimuthal angle would be visible to ANITA given the payload latitude.

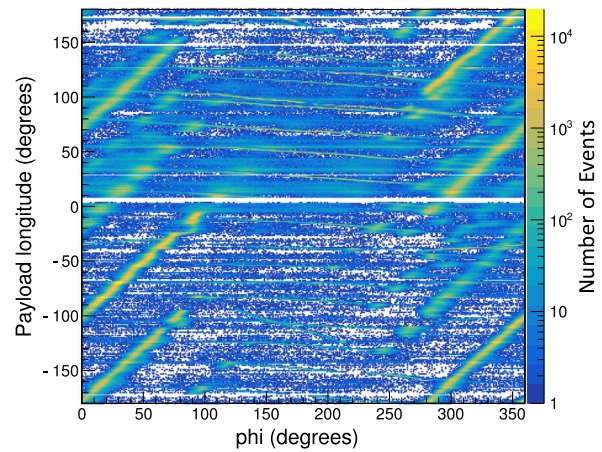


FIG. 12. The longitude of the ANITA-III payload as a function of reconstructed angle in azimuth, corrected for payload heading, derived from the cross-correlation of LCP waveforms. CW signals from geosynchronous satellites appear as an excess of events along lines with a slope of unity. Stripes are faint near  $\phi = 180^\circ$ , where the reconstructed location is toward the South Pole.

Whereas analyses A and B use selection criteria with a focus on measures of impulsivity of the signals, one way in which Analysis C is complementary is its focus on peak cross-correlation values. Figure 13 shows a two-dimensional distribution of the voltage SNR of the coherently summed waveform plotted against the peak value of the cross-correlation coefficient of events reconstructing to one of the geographic bins in the ANITA-III data set. All events below the red line in the plot are cut. A common slope for the cut line was used across all bins at  $-6$  (unitless) as in Fig. 13, since at an early stage of the analysis it was found to produce the best expected limit. A unique and optimum

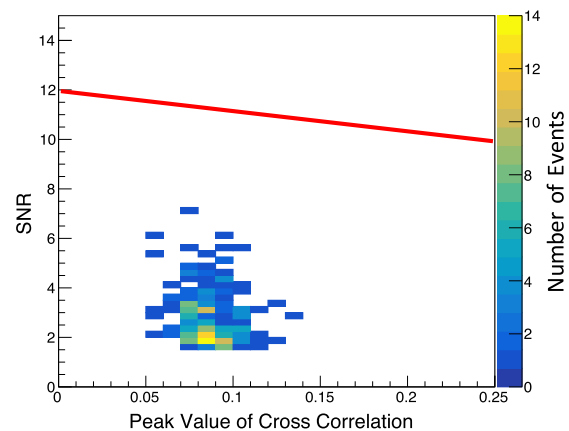


FIG. 13. The voltage SNR of the coherently summed waveform as a function of peak cross-correlation value for events in the 10% data set of ANITA-III used in Analysis C, reconstructing to HEALPix bin 2970, in the vertical polarization analysis. The red line shows the LD cut for this bin.

placement of the Linear Discriminant (LD) cut is calculated for each bin, as described in Appendix C 3.

### 2. Ice selection and clustering

With the aim of keeping as much ice as possible, in Analysis C, 37 and 29 HEALPix bins are kept for the horizontally and vertically polarized (HPol and VPol) channels, respectively, corresponding to bins that include 61% and 73% of the neutrino sensitivity for the VPol and HPol channels, respectively, at the stage in which the LD cut is imposed.

In each bin where Analysis C performs its search, events from a 10% sample are used to obtain the background estimate for that bin by fitting to an exponential function in a variable that represents the position of the LD cut as shown in Fig. 14. Figure 15 shows the background and signal expectation in each bin used. Bins are removed if

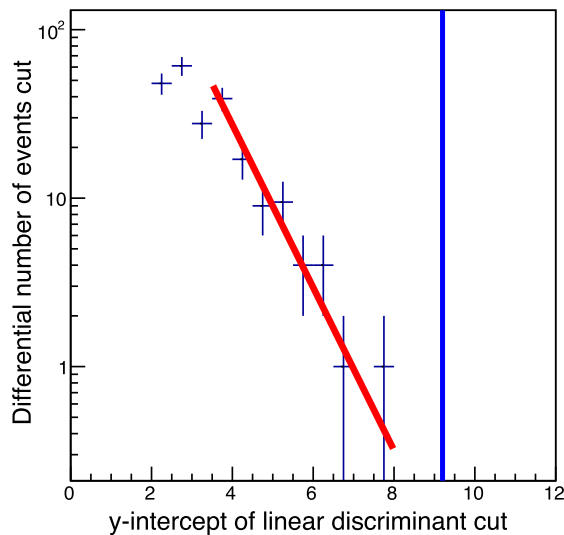


FIG. 14. The distribution of events as a function of position of the linear discriminant cut from the 10% data set in Analysis C for bin 2970 in the VPol channel of the analysis. The blue vertical line shows the position of the cut in this bin found by the optimization procedure.

there are not sufficient data beyond the peak to fit (at least five events across five bins). We also require that the exponential fit returns a p value between 0.05 and 0.999. Moreover, we rank the bins in order of simulated sensitivity to neutrinos and place bins in the lowest one percentile in a sideband region.

For a final step in the analysis, we reject events that pass all other cuts but cluster with any other horizontally or vertically polarized events. In the vertically polarized channel, in seven bins, we reject events that cluster with at least one other event, consistent with sampling from just 10% of the data to predict the backgrounds. Based on the observed clusters in the 90% signal region, we determine postunblinding that we expect a 2.2 “singlet” (single events not paired with any others during clustering) background among all VPol and HPol bins, in addition to the preunblinding background estimates.

Table IV shows the efficiencies of the cuts used in Analysis C on simulated neutrinos as well as the 90% data set. We note that our quality cuts are less efficient compared to the other two analyses (62%) due to aggressively cutting away regions where satellites are present and in directions where our trigger was masked. In addition, the analysis cuts for Analysis C rely on high cross-correlation values between waveforms with common fields of view rather than impulsivity, and while this adds a complementarity between analyses, the requirement is on average only 20% efficient. This cut varies between bins and is more efficient in some areas.

### 3. Optimization and systematic uncertainties

We optimize in the VPol and HPol channels separately, in each case for the best constraint on the chosen neutrino flux, despite only considering the VPol channel for our Askaryan neutrino search. The optimization consists of a few steps, and at every stage, to calculate the expected limit for a given set of LD cuts and orientation, we follow a Bayesian technique with a flat prior on  $C$ , a scale factor on the Kotera model, with proper smearing of backgrounds to account for systematic uncertainties.

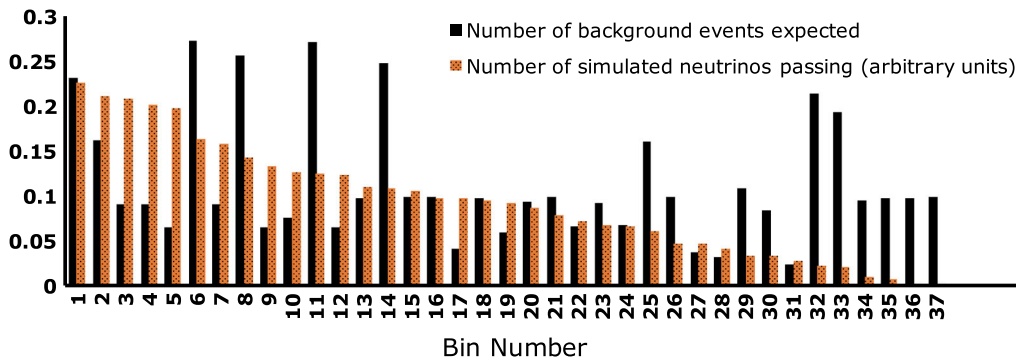


FIG. 15. The background estimate and number of expected events from the Kotera model in each bin of ice used in Analysis C.

TABLE IV. Neutrino efficiencies and events kept for each stage of cuts (not cumulative) from the 90% data set at each stage of Analysis C. Efficiencies are the geometric average from two MC samples, one containing the local noise environment in analysis chain only and another with simulated thermal noise.

Cut	MC $\nu$ efficiency cut by each (%)	Comments	Events kept
Total	100		$5.9 \times 10^7$
Quality cuts	62		$3.8 \times 10^5$
Event selection	99		$1.7 \times 10^5$
Bin selection	61		$8.8 \times 10^4$
Final selection	19	Range 4.4%–29%	67
Clustering	98	7 bins affected	2

First, for a given orientation of the HEALPix map, the LD cut for each bin is optimized for the best constraint on the Kotera model from that bin alone. Next, given those LD cuts, the bins are combined to obtain an expected limit on  $C$ , a scale factor for the Kotera model. Then, all LD cuts are moved up and down together for the best expected constraint  $C$ . Finally, all of this is repeated for orientations covering a  $10 \times 10$  grid in latitude and longitude shifts within one bin increment of the HEALPix map in order to obtain the set of LD cuts and orientations that give the best expected constraint  $C$ .

For a single bin, in the absence of systematic uncertainties, for an expected background  $b$  and signal events  $s$ , a 90% C.L. upper limit can be placed on the number of signal events  $s_{\text{up}}$  that satisfies

$$0.1 < \frac{\int_{s_{\text{up}}}^{\infty} e^{-(b+s)} (b+s)^b ds}{\int_0^{\infty} e^{-(b+s)} (b+s)^b ds}. \quad (\text{C1})$$

We can create a combined limit over many bins; the relative number of signal events across bins is set by simulation, and we find a scale factor on the overall flux,  $C$ , as

$$0.1 < \frac{\int_{s_{\text{up}}}^{\infty} \prod_i \int P_i(b) db e^{-(b+C s_i)} (b+C s_i)^b ds}{\int_0^{\infty} \prod_i \int P_i(b) db e^{-(b+C s_i)} (b+C s_i)^b ds}. \quad (\text{C2})$$

Analysis C used three different systematic uncertainties as a function of cut values in its optimization procedure [18]. Although these uncertainties undoubtedly led to conservative cuts with reduced backgrounds, postunblinding, we found that these systematic uncertainties were overestimated. Therefore, we set our measured limit based on statistical errors and uncertainties on exponential fits only.

The three different uncertainties included in the optimization were 1) errors on parameters of the exponential fit for modeling the background (calculated to be a few

percent), 2) the choice of functional form for modeling background (our dominant uncertainty at tens of percent), and 3) spillover of events between neighboring bins due to imperfect resolution on the reconstruction direction (negligible for nearly all bins). To assess the uncertainty due to the choice of fit, we fit the data in the 10% sample to a power-law function in each bin, in addition to the exponential.

When finding the measured limit on a specific model, we account for our estimated singlet background (see Appendix C 2), by generating singlets from a Poisson distribution with a mean of  $2.2 \pm 0.6$ , and distribute them with equal probability among all bins in the vertical and horizontal polarization channels, consistent with how observed clusters are distributed in Analysis C. We set a constraint  $C$  that is a factor of 8.7 higher than Analysis B. However, demonstrating the potential for complementing the other analyses, 25% of neutrinos seen by Analysis C would have been rejected by the others.

#### 4. Discussion

With the aim of maintaining sensitivity to neutrinos when viewing ice where anthropogenic noise is present, Analysis C took an aggressive approach at background mitigation and, together with a choice of complementary analysis variables, has a lower efficiency for the search for a diffuse neutrino flux than the other analyses at present. For the analysis of data from the fourth flight of ANITA (ANITA-IV), the focus will be to improve efficiencies without allowing more background to pass.

We note that this approach of searching in bins of ice is well suited for neutrinos from astrophysical transient sources such as gamma-ray bursts. For a given transient, the neutrinos would be expected only from a localized region of ice for a short period of time. Restricting the search region in both time and direction in this way allows for lower analysis thresholds for the same background level.

#### APPENDIX D: LIMIT CALCULATION

The ANITA-III 90% confidence level limit on the all-flavor-sum diffuse neutrino flux is set by using

$$\left( \frac{Ed^4N}{dEdA d\Omega dt} \right)_{\text{lim}} = \frac{s_{\text{up}}}{T \cdot \epsilon_{\text{ana}}(E_\nu) \cdot \langle A\Omega \rangle(E) \cdot \Delta}, \quad (\text{D1})$$

where  $s_{\text{up}}$  is the upper side of the Feldman-Cousins confidence interval integrated over the systematic error on the background, for the mean of a Poisson variable given the number of observed events and the estimated background. The lower side of the Feldman-Cousins confidence interval in our case is 0. For Analysis B, with one event observed and a background estimate of  $0.7_{-0.3}^{+0.5}$ , we calculate  $s_{\text{up}} = 3.47$ .

The live time for ANITA-III is  $T = 17.4$  days, which includes the digitization dead time but not channel masking effects, which are included in the calculation of the acceptance.  $\epsilon_{\text{ana}}(E_\nu)$  is the Analysis B neutrino analysis efficiency as a function of energy. The experiment acceptance,  $\langle A\Omega \rangle(E)$ , is calculated with a weighted Monte Carlo [13] and using the approximation

$$\langle A\Omega \rangle(E) = \frac{\langle V\Omega \rangle(E)}{\ell_{\text{int}}(E)}, \quad (\text{D2})$$

where  $\langle V\Omega \rangle(E)$  is the volumetric acceptance and  $\ell_{\text{int}}(E)$  is the neutrino interaction length calculated from Ref. [14]. The values of the ANITA-III acceptance are found in Fig. 6. Finally, the factor  $\Delta = 4$  follows the normalization convention in Appendix B of Ref. [30], which was derived by considering a typical range in log-energy space of the spectrum that follows a  $1/E$  distribution.

The combined limit for ANITA I-III is calculated using the total number of events seen, total expected background, and the analysis-efficiency-weighted sum of previously published effective volumes [8].

- 
- [1] V. S. Beresinsky and G. T. Zatsepin, *Phys. Lett. B* **28**, 423 (1969).
- [2] K. Kotera, D. Allard, and A. V. Olinto, *J. Cosmol. Astropart. Phys.* **10** (2010) 013.
- [3] G. Askaryan, *Sov. Phys. J. Exp. Theor. Phys.* **14**, 441 (1962).
- [4] P. W. Gorham *et al.*, *Astropart. Phys.* **32**, 10 (2009).
- [5] S. Hoover *et al.* (ANITA Collaboration), *Phys. Rev. Lett.* **105**, 151101 (2010).
- [6] P. W. Gorham *et al.* (ANITA Collaboration), *Phys. Rev. Lett.* **117**, 071101 (2016).
- [7] P. W. Gorham *et al.* (ANITA Collaboration), *Phys. Rev. Lett.* **103**, 051103 (2009).
- [8] P. W. Gorham *et al.* (ANITA Collaboration), *Phys. Rev. D* **82**, 022004 (2010); **85**, 049901(E) (2012).
- [9] G. S. Varner, L. L. Ruckman, J. W. Nam, R. J. Nichol, J. Cao, P. W. Gorham, and M. Wilcox, *Nucl. Instrum. Methods Phys. Res., Sect. A* **583**, 447 (2007).
- [10] P. Fretwell *et al.*, *Cryosphere* **7**, 375 (2013).
- [11] B. Strutt, Ph. D. thesis, University College London, 2016.
- [12] B. Rotter, Ph. D. thesis, University of Hawai'i, 2017.
- [13] L. Cremonesi *et al.* (ANITA Collaboration) (to be published).
- [14] A. Connolly, R. Thorne, and D. Waters, *Phys. Rev. D* **83**, 113009 (2011).
- [15] B. Dailey, Ph. D. thesis, The Ohio State University, 2016.
- [16] A. Romero-Wolf *et al.* (ANITA Collaboration), *Astropart. Phys.* **60**, 72 (2015).
- [17] K. M. Gorski, E. Hivon, A. J. Banday, B. D. Wandelt, F. K. Hansen, M. Reinecke, and M. Bartelmann, *Astrophys. J.* **622**, 759 (2005).
- [18] J. Gordon, Ph. D. thesis, The Ohio State University, 2018.
- [19] S. Stafford, Ph. D. thesis, The Ohio State University, 2017.
- [20] W. Rolke, A. Lopez, and J. Conrad, *Nuclear Instruments and Methods A* **551**, 493 (2005).
- [21] P. Gorham *et al.* (ANITA Collaboration), [arXiv:1803.05088](https://arxiv.org/abs/1803.05088).
- [22] A. Aab *et al.* (Pierre Auger Collaboration), *Phys. Rev. D* **91**, 092008 (2015).
- [23] M. G. Aartsen *et al.*, *Phys. Rev. Lett.* **119**, 259902 (2017).
- [24] M. Ahlers and F. Halzen, *Phys. Rev. D* **86**, 083010 (2012).
- [25] R. A. Fisher, *Ann. Eugen.* **7**, 179 (1936).
- [26] A. Hoecker *et al.*, *Proc. Sci. ACAT2007* (**2007**) 040.
- [27] A. Bhattacharyya, *Sankhy* **7**, 401 (1946).
- [28] L. Moneta *et al.*, *Proc. Sci. ACAT2010* (**2010**) 057.
- [29] P. W. Gorham *et al.* (ANITA Collaboration), *J. Astron. Inst.* **6**, 1740002 (2017).
- [30] I. Kravchenko *et al.* (RICE Collaboration), *Phys. Rev. D* **73**, 082002 (2006).